This article has been accepted for publication in a future issue of this journal, but has not been fully edited. Content may change prior to final publication.
Citation information: DOI: 10.1109/TVT.2025.3640407, IEEE Transactions on Vehicular Technology

On the Performance Analysis of Pinching-Antenna-Enabled SWIPT Systems

Bingxin Zhang, *Member, IEEE,* Han Zhang, *Student Member, IEEE,* Kun Yang, *Fellow, IEEE,* Yizhe Zhao, *Member, IEEE,* and Kezhi Wang, *Senior Member, IEEE*

***Abstract*—In this paper, we study the performance of a novel simultaneous wireless information and power transfer (SWIPT) system assisted by a flexible pinching antenna. To enable practical deployment and enhance the energy–rate trade-off performance, three pinching antenna placement schemes are proposed, namely the edge deployment scheme (EDS), the center deployment scheme (CDS), and the diagonal deployment scheme (DDS). In addition, a hybrid time-switching (TS) and power-splitting (PS) protocol is introduced to dynamically balance energy harvesting and information decoding. For each deployment strategy, closed-form expressions for the average harvested energy and achievable rate of a randomly located user equipment (UE) are derived based on the optimal antenna position along the waveguide. Numerical results validate the analytical expressions and demonstrate the inherent trade-off between information rate and harvested energy under different deployment schemes.**

***Index Terms*—Pinching antenna, simultaneous wireless information and power transfer, rate-energy region, performance analysis.**

I. Introduction

The rapid growth of wireless data traffic and the emergence of energy-constrained devices in 6G networks have necessitated the integration of simultaneous wireless information and power transfer (SWIPT) into communication systems [1]. However, existing SWIPT techniques face significant challenges when deployed in complex environments with severe path loss or non-line-of-sight (NLoS) conditions. To address these issues, several flexible antenna architectures have been proposed in recent years, including intelligent reflecting surfaces (IRS) [2], fluid antennas [3], and movable antennas [4]. IRSs can construct virtual line-of-sight (LoS) links by intelligently reflecting signals. However, its performance is inherently limited by the double-fading effect. Fluid antennas and movable antennas provide physical relocation capability; however, their movement range is typically constrained within a few wavelengths, making them ineffective against large-scale fading or user mobility over extended areas.

To overcome these limitations, a novel concept referred to as the pinching antenna has been proposed by NTT DOCOMO [5], which enables dynamic channel configuration by physically placing a dielectric "clip" at arbitrary positions along a flexible waveguide. This promising architecture is expected to play a key role in future wireless systems by enhancing line-of-sight connectivity, mitigating large-scale fading, and enabling reconfigurable antenna deployment tailored to user mobility and energy demands [6]. Although the research on pinching antennas is still in its early stages, several initial studies have been conducted to explore their fundamental properties and performance in wireless systems [7]–[10].

Specifically, for SWIPT systems, the pinching antenna offers three key advantages: (i) flexible configurability that enables adaptive near-field LoS link formation, (ii) significant reduction of large-scale propagation loss by extending the waveguide closer to target devices, and (iii) cost-effective hardware implementation requiring only simple insertion or removal of dielectric particles. With these properties, the pinching antenna is particularly suitable for SWIPT systems that demand efficient and reconfigurable LoS transmission. Recent works have broadly investigated pinching antenna position optimization [11], the design of multiple-access transmission strategies [12], and channel modeling under probabilistic LoS blockage [13].

However, existing studies on pinching antenna-assisted SWIPT systems have primarily focused on optimization-based design, while their fundamental performance limits have not been thoroughly analyzed. Moreover, the impact of different waveguide deployment schemes on system performance has not been investigated in the literature. Motivated by these observations, this paper provides a detailed performance analysis of pinching antenna-assisted SWIPT systems. Specifically, the main contributions are summarized as follows: (i) We introduce the pinching antenna into the SWIPT framework and propose three waveguide deployment schemes; (ii) For each deployment scheme, we derive novel closed-form expressions for the average harvested energy and average achievable rate under both linear energy harvesting model (LM) and non-linear energy harvesting model (NLM), offering analytical insights into the energy-rate trade-off; (iii) Extensive Monte Carlo simulations validate the accuracy of the derived ex-

This paper was partly funded by Jiangsu Major Project on Fundamental Researches (Grant No.: BK20243059), Gusu Innovation Project for People (Grant No.: ZXL2024360), Natural Science Foundation of China (Grant No. 62531008, 62132004) and Nanjing University-China Mobile Communications Group Co.,Ltd. Joint Institute. (*Corresponding author: Kun Yang.*)

Bingxin Zhang, Han Zhang and Kun Yang are with the State Key Laboratory of Novel Software Technology, Nanjing University, Nanjing, 210008, China, Institute of Intelligent Networks and Communications (NINE), Collaborative Innovation Center of Novel Software Technology and Industrialization, and School of Intelligent Software and Engineering, Nanjing University (Suzhou Campus), Suzhou, 215163, China (email: bxzhang@nju.edu.cn; hanzhangl@smail.nju.edu.cn; kunyang@nju.edu.cn).

Yizhe Zhao is with the School of Information and Communication Engineering, University of Electronic Science and Technology of China, Chengdu 611731, China (e-mail: yzzhao@uestc.edu.cn).

Kezhi Wang is with Department of Computer Science, Brunel University London, Uxbridge, Middlesex, UB8 3PH (email: kezhi.wang@brunel.ac.uk).

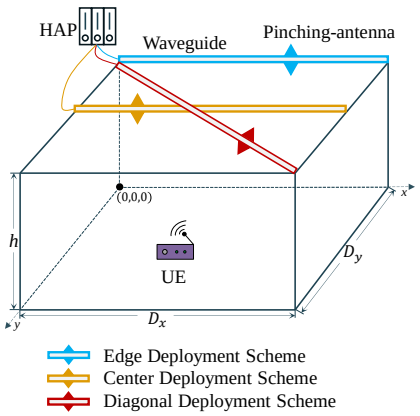

Fig. 1. System model of the pinching-antenna-enabled SWIPT system.

pressions and reveal how waveguide deployment schemes and transmission protocol parameters influence the trade-off between rate and energy performance.

II. System Model

As illustrated in Fig. 1, we consider a SWIPT system in which a hybrid access point (HAP) serves a single-antenna user equipment (UE). In particular, the UE is assumed to be randomly located within a rectangular region on the x–y plane, with side lengths D_x and D_y along the x- and y-axes, respectively. The UE's position is denoted by $\boldsymbol{\psi}_{\mathrm{u}} = (x_{\mathrm{u}}, y_{\mathrm{u}}, 0)$, where $x_{\mathrm{u}} \sim \mathcal{U}[0, D_x]$ and $y_{\mathrm{u}} \sim \mathcal{U}[0, D_y]$. To ensure robust information and energy transmission, the HAP employs a pinching antenna integrated with a dielectric waveguide, enabling dynamic adjustment of the antenna's position along the waveguide to optimize the wireless transmission link. Unlike conventional wireless architectures, the pinching antenna system facilitates low-loss propagation of high-frequency signals within the waveguide and enables controlled radiation at arbitrary locations along its length via a "pinching" mechanism. Specifically, the waveguide is deployed at a height h, and the positions of the HAP and the pinching antenna are given by $\boldsymbol{\psi}_{\mathrm{b}} = (0, 0, h)$ and $\boldsymbol{\psi}_{\mathrm{p}} = (x_{\mathrm{p}}, y_{\mathrm{p}}, h)$, respectively. It is worth noting that three waveguide deployment schemes are proposed, namely the edge deployment scheme, the center deployment scheme, and the diagonal deployment scheme, as depicted in Fig. 1. The detailed configurations of each scheme will be discussed in Section III.

Furthermore, to capture the full trade-off between energy harvesting and information transmission, and thereby provide a more comprehensive performance characterization, a hybrid time-switching (TS) and power-splitting (PS) protocol is adopted in this work. In particular, the transmission duration is denoted by T. During the αT portion of the transmission period, a fraction β of the received power is allocated for energy harvesting, while the remaining $(1-\beta)$ portion is used for information decoding. In the remaining $(1-\alpha)T$ period, the entire received power is utilized for information decoding. In this scheme, the parameters $\alpha \in [0,1]$ and $\beta \in [0,1]$ correspond to the TS factor and PS factor, respectively. It is worth noting that when $\alpha = 1$, the hybrid protocol reduces to the PS scheme, while when $\beta = 1$, it reduces to the TS scheme. To facilitate analysis, T is normalized to 1.

Therefore, when the LoS link is unobstructed, the received signal at the UE can be given by

$$y = \frac{\sqrt{\mu P_t} e^{-j\frac{2\pi}{\lambda}\left\|\boldsymbol{\psi}_{\mathrm{p}} - \boldsymbol{\psi}_{\mathrm{u}}\right\|}}{\left\|\boldsymbol{\psi}_{\mathrm{p}} - \boldsymbol{\psi}_{\mathrm{u}}\right\|} s + n, \tag{1}$$

where $\mu = \frac{c^2}{16\pi^2 f_c^2}$, c represents the speed of light, f_c denotes the carrier frequency, P_t represents the transmit power, λ is the free-space wavelength, $\left\|\boldsymbol{\psi}_{\mathrm{p}} - \boldsymbol{\psi}_{\mathrm{u}}\right\|$ denotes the distance between the pinching antenna and the UE, s is the transmitted signal by the BS satisfying $\mathbb{E}\left[|s|^2\right] = 1$, and $n \sim \mathcal{CN}(0, \sigma^2)$ denotes the additive white Gaussian noise with zero mean and variance σ^2.

However, LoS transmission is often subject to random blockages caused by obstacles or user mobility, a phenomenon that becomes particularly pronounced in high-frequency bands such as mmWave and THz. To characterize this uncertainty, we employ a probabilistic LoS blockage model, where the LoS state is described by a Bernoulli random variable $\xi \in \{0, 1\}$. Specifically, $\xi = 1$ denotes an unobstructed LoS path. The LoS probability can be defined as

$$\Pr(\xi = 1) = e^{-\delta\left\|\boldsymbol{\psi}_{\mathrm{p}} - \boldsymbol{\psi}_{\mathrm{u}}\right\|^2}, \tag{2}$$

where $\delta > 0$ is the blockage density parameter that reflects the level of environmental clutter.

Then, for energy harvesting, based on the transmission protocol and assuming a LM, the average harvested energy at the UE can be expressed as

$$\bar{E}_{\mathrm{LM}} = \mathbb{E}\left[\frac{\alpha\beta\eta P_t e^{-\delta\left\|\boldsymbol{\psi}_{\mathrm{p}} - \boldsymbol{\psi}_{\mathrm{u}}\right\|^2}}{\left\|\boldsymbol{\psi}_{\mathrm{p}} - \boldsymbol{\psi}_{\mathrm{u}}\right\|^2}\right], \tag{3}$$

where $\eta \in (0, 1)$ denotes the energy conversion efficiency coefficient of the UE's rectifying antenna.

In practice, the energy harvesting circuits in the UE typically exhibit non-linear characteristics due to components like diodes or capacitors. To more accurately describe the actual energy harvesting process, a logistic model is widely adopted. Under the NLM, the energy harvested at the UE can be redefined as

$$\Phi(P_{\mathrm{in}}) = \left[\frac{\varphi}{1-\Omega}\left(\frac{1}{1+e^{-a(P_{\mathrm{in}}-b)}} - \Omega\right)\right]^+, \tag{4}$$

where $[x]^+ = \max(0, x)$, $\Omega = \frac{1}{1+e^{ab}}$ and P_{in} represents the incident power. In addition, φ denotes the maximum harvested power under energy harvesting saturation, while a and b characterize the circuit behavior determined by components such as diodes and resistors. By adjusting these parameters, different energy harvesting circuit configurations can be represented.

Consequently, by adopting the NLM in (4), the average energy harvested at the UE can be written as

$$\bar{E}_{\mathrm{NLM}} = \alpha\mathbb{E}\left[\Phi(P_{\mathrm{in}})\right], \tag{5}$$

where $P_{\mathrm{in}} = \frac{\beta P_t e^{-\delta\left\|\boldsymbol{\psi}_{\mathrm{p}} - \boldsymbol{\psi}_{\mathrm{u}}\right\|^2}}{\left\|\boldsymbol{\psi}_{\mathrm{p}} - \boldsymbol{\psi}_{\mathrm{u}}\right\|^2}$.

According to (1) and (2), the received signal-to-noise ratio (SNR) at the UE can be expressed as

$$\gamma = \frac{\mu P_t e^{-\delta \left\| \boldsymbol{\psi}_{\mathrm{p}} - \boldsymbol{\psi}_{\mathrm{u}} \right\|^2}}{\left\| \boldsymbol{\psi}_{\mathrm{p}} - \boldsymbol{\psi}_{\mathrm{u}} \right\|^2 \sigma^2}. \tag{6}$$

With respect to information decoding, according to the hybrid transmission protocol, the average achievable rate at the UE can be defined as

$$\begin{aligned} \bar{R} &= [\alpha(1-\beta) + (1-\alpha)]\, \mathbb{E}\left[\log_2\left(1+\gamma\right)\right] \\ &= (1-\alpha\beta)\mathbb{E}\left[\log_2\left(1 + \frac{\mu\bar{\gamma} e^{-\delta \left\| \boldsymbol{\psi}_{\mathrm{p}} - \boldsymbol{\psi}_{\mathrm{u}} \right\|^2}}{\left\| \boldsymbol{\psi}_{\mathrm{p}} - \boldsymbol{\psi}_{\mathrm{u}} \right\|^2}\right)\right], \end{aligned} \tag{7}$$

where $\bar{\gamma} = \frac{P_t}{\sigma^2}$.

III. Performance Analysis

In the investigated pinching-antenna-enabled SWIPT system, we propose three waveguide deployment schemes:

- **Edge Deployment Scheme (EDS):** The waveguide is deployed at height h, aligned parallel to the x-axis, with a fixed y-coordinate of 0. Accordingly, the coordinate of the pinching antenna is denoted as $(x_{\mathrm{p},1}, 0, h)$, where $x_{\mathrm{p},1} \in [0, D_x]$.
- **Central Deployment Scheme (CDS):** The waveguide is deployed at height h, also parallel to the x-axis, but fixed at $y = \frac{D_y}{2}$. The corresponding pinching antenna coordinate is given by $(x_{\mathrm{p},2}, \frac{D_y}{2}, h)$, where $x_{\mathrm{p},2} \in [0, D_x]$.
- **Diagonal Deployment Scheme (DDS):** The waveguide is deployed along the top diagonal direction at height h, and the pinching antenna position is expressed as $(x_{\mathrm{p},3}, y_{\mathrm{p},3}, h)$, where $x_{\mathrm{p},3} \in [0, D_x]$, $y_{\mathrm{p},3} = \frac{D_y}{D_x} x_{\mathrm{p},3}$.

The EDS corresponds to waveguides deployed along walls, typical for boundary-mounted infrastructure. The CDS models deployment along the corridor center or the central axis of a rectangular area, ensuring balanced coverage on both sides. The DDS denotes diagonal deployment across corridors or rectangular areas, providing flexible coverage and reducing the average distance to users randomly distributed in the two-dimensional region. These three schemes capture practical and reasonable deployment strategies in typical indoor scenarios.

To evaluate the performance of the average harvested energy and average achievable rate, it is essential to first characterize the distribution of the squared distance between the pinching antenna and the UE under the three waveguide deployment schemes, denoted as $L_\nu = \left\| \boldsymbol{\psi}_{\mathrm{p},\nu} - \boldsymbol{\psi}_{\mathrm{u}} \right\|^2$, where $\nu \in \{1, 2, 3\}$.

Leveraging the flexibility of the pinching antenna, it is strategically positioned as close to the UE as possible to maximize the SWIPT performance by minimizing the impact of large-scale fading. Accordingly, under the EDS and CDS configurations, the optimal pinching antenna positions are denoted by $\boldsymbol{\psi}^*_{\mathrm{p},1} = (x_{\mathrm{u}}, 0, h)$ and $\boldsymbol{\psi}^*_{\mathrm{p},2}(x_{\mathrm{u}}, \frac{D_y}{2}, h)$, respectively. For the DDS, the squared distance between the pinching antenna and the UE is derived as

$$\begin{aligned} L_3 &= \left\| \boldsymbol{\psi}_{\mathrm{p},3} - \boldsymbol{\psi}_{\mathrm{u}} \right\|^2 = \left(x_{\mathrm{p},3} - x_{\mathrm{u}}\right)^2 + \left(k x_{\mathrm{p},3} - y_{\mathrm{u}}\right)^2 + h^2 \\ &= (1+k^2) x_{\mathrm{p},3}^2 - 2(x_{\mathrm{u}} + k y_{\mathrm{u}}) x_{\mathrm{p},3} + (x_{\mathrm{u}}^2 + y_{\mathrm{u}}^2 + h^2), \end{aligned} \tag{8}$$

where $k = \frac{D_y}{D_x}$.

Then, by taking the derivative of $x_{\mathrm{p},3}$ in (8) and setting it to zero, i.e., $\frac{dL_3}{dx_{\mathrm{p},3}} = 0$, we obtain

$$x^*_{\mathrm{p},3} = \frac{x_{\mathrm{u}} + k y_{\mathrm{u}}}{1+k^2} \quad \text{and} \quad y^*_{\mathrm{p},3} = \frac{k x_{\mathrm{u}} + k^2 y_{\mathrm{u}}}{1+k^2}. \tag{9}$$

Accordingly, the optimal position of the pinching antenna under the DDS is given by $\boldsymbol{\psi}^*_{\mathrm{p},3} = (x^*_{\mathrm{p},3}, y^*_{\mathrm{p},3}, h)$.

Then, based on the optimal pinching antenna configurations under the three deployment schemes, the cumulative distribution function (CDF) and probability density function (PDF) of the random variable L^*_ν, with $\nu \in \{1, 2, 3\}$, will be presented in the following two lemmas.

Lemma 1. For the EDS and CDS, the CDF and PDF of the random variable L_ϖ are given by

$$F_{L^*_\varpi}(l) = \begin{cases} 0, & l < h^2, \\ \frac{\varpi\sqrt{l-h^2}}{D_y}, & h^2 \le l \le h^2 + \left(\frac{D_y}{\varpi}\right)^2, \\ 1, & l > h^2 + \left(\frac{D_y}{\varpi}\right)^2, \end{cases} \tag{10}$$

and

$$f_{L^*_\varpi}(l) = \begin{cases} \frac{\varpi}{2D_y\sqrt{l-h^2}}, & h^2 \le l \le h^2 + \left(\frac{D_y}{\varpi}\right)^2, \\ 0, & \text{otherwise}, \end{cases} \tag{11}$$

respectively, $\varpi \in \{1, 2\}$.

Proof: We first analyze the CDF of the minimum distance L^*_1 between the pinching antenna and the UE under the EDS. Therefore, one has

$$L^*_1 = y^2_{\mathrm{u},1} + h^2. \tag{12}$$

Then, given that $y_{\mathrm{u}} \sim \mathcal{U}[0, D_y]$ and the definition $F_{L^*_1}(l) = \Pr\{L^*_1 \le l\}$, the CDF of L^*_1 can be readily obtained as shown in (10). Furthermore, taking the first-order derivative of (10) with respect to l yields the PDF of L^*_1, as given in (11). Finally, the CDF and PDF of the random variable L^*_2 can be obtained using a method similar to that of L^*_1. ■

Lemma 2. For the DDS, the CDF and PDF of L_3 can be derived as

$$F_{L^*_3}(l) = \begin{cases} 0, & l < h^2, \\ \frac{2\Lambda\sqrt{l-h^2} - l + h^2}{\Lambda^2}, & h^2 \le l \le h^2 + \Lambda^2, \\ 1, & l > h^2 + \Lambda^2, \end{cases} \tag{13}$$

and

$$f_{L^*_3}(l) = \begin{cases} \frac{1}{\Lambda\sqrt{l-h^2}} - \frac{1}{\Lambda^2}, & h^2 \le l \le h^2 + \Lambda^2, \\ 0, & \text{otherwise}, \end{cases} \tag{14}$$

respectively, where $\Lambda = \frac{D_x D_y}{\sqrt{D_x^2 + D_y^2}}$.

Proof: Please refer to Appendix A. ■

Lemma 3. For the EDS and CDS, the average harvested energy at the UE under the LM can be expressed as

$$\bar{E}_{\mathrm{LM},\varpi} = \frac{\pi\alpha\beta\eta P_t e^{-\delta h^2}}{2\mathcal{M}} \sum_{m=1}^{\mathcal{M}} \frac{\sqrt{1-x_m^2}\, e^{-\delta y_m^2}}{h^2 + y_m^2}, \tag{15}$$

where $y_m = \frac{D_y x_m}{2\varpi} + \frac{D_y}{2\varpi}$, $\varpi \in \{1, 2\}$, $x_m = \cos\left(\frac{(2m-1)\pi}{2\mathcal{M}}\right)$, and $\mathcal{M}$ is a finite value.

Proof: Based on (3) and (11), one has

$$\begin{aligned}\bar{E}_{\mathrm{LM},\varpi} &= \alpha\beta\eta P_t \mathbb{E}\left[\frac{e^{-\delta L_{\varpi}^{*}}}{L_{\varpi}^{*}}\right] \\ &\overset{(a)}{=} \frac{\alpha\beta\eta P_t \varpi e^{-\delta h^2}}{D_y}\int_0^{\frac{D_y}{\varpi}} \frac{e^{-\delta t^2}}{h^2+t^2}\mathrm{d}t,\end{aligned} \tag{16}$$

where step (a) follows from the variable substitution $l = h^2 + t^2$. However, it is difficult to obtain an exact closed-form expression for (16). Therefore, the Gaussian–Chebyshev quadrature method [15] is employed to derive an approximate closed-form expression for (15) that is suitable for engineering applications. ∎

Lemma 4. For the DDS, the average harvested energy at the UE under the LM can be derived as

$$\begin{aligned}\bar{E}_{\mathrm{LM},3} = \frac{\alpha\beta\eta P_t \Lambda^2 \pi}{2\mathcal{M}} \sum_{m=1}^{\mathcal{M}} \sqrt{1-x_m^2} \\ \left(\frac{e^{-\delta y_m}}{\Lambda y_m \sqrt{y_m - h^2}} - \frac{e^{-\delta y_m}}{\Lambda^2 y_m}\right),\end{aligned} \tag{17}$$

where $y_m = \frac{\Lambda^2 x_m}{2} + \frac{2h^2+\Lambda^2}{2}$, $x_m = \cos\left(\frac{(2m-1)\pi}{2\mathcal{M}}\right)$.

Proof: Under the DDS configuration, we have

$$\bar{E}_{\mathrm{LM},3} = \alpha\beta\eta P_t \underbrace{\int_{h^2}^{h^2+\Lambda^2} \frac{e^{-\delta l}}{\Lambda l\sqrt{l-h^2}} - \frac{e^{-\delta l}}{\Lambda^2 l}\mathrm{d}l}_{I_1}. \tag{18}$$

Then, the integral I_1 in (18) can be obtained using a similar approach to that in (16) as

$$I_1 = \frac{\Lambda^2\pi}{2\mathcal{M}} \sum_{m=1}^{\mathcal{M}} \sqrt{1-x_m^2}\left(\frac{e^{-\delta y_m}}{\Lambda y_m\sqrt{y_m-h^2}} - \frac{e^{-\delta y_m}}{\Lambda^2 y_m}\right), \tag{19}$$

where $y_m = \frac{\Lambda^2 x_m}{2} + \frac{2h^2+\Lambda^2}{2}$, $x_m = \cos\left(\frac{(2m-1)\pi}{2\mathcal{M}}\right)$, and $\mathcal{M}$ is a finite value.

Finally, by substituting (19) into equation (18), (17) can be obtained. ∎

Next, we present an upper bound on the average harvested energy of the UE under the NLM, as given in the following lemma.

Lemma 5. Based on the proposed three waveguide deployment schemes and the transmission protocol, an upper bound on the average harvested energy at the UE under the NLM can be expressed as

$$\hat{E}_{\mathrm{NLM},\nu} = \alpha\Phi\left(P_{\mathrm{in},\nu}\right), \quad \nu \in \{1,2,3\}, \tag{20}$$

where $P_{\mathrm{in},\varpi} = \frac{\pi\beta P_t e^{-\delta h^2}}{2\mathcal{M}} \sum_{m=1}^{\mathcal{M}} \frac{\sqrt{1-x_m^2}e^{-\delta y_m^2}}{h^2+y_m^2}$, $P_{\mathrm{in},3} = \frac{\beta P_t \Lambda^2 \pi}{2\mathcal{M}} \sum_{m=1}^{\mathcal{M}} \sqrt{1-x_m^2}\left(\frac{e^{-\delta y_m^2}}{\Lambda y_m\sqrt{y_m-h^2}} - \frac{e^{-\delta y_m}}{\Lambda^2 y_m}\right)$, the parameters x_m and y_m are defined in equations (15) and (17), respectively.

Proof: For the NLM, due to $\Phi\left(P_{\mathrm{in}}\right)$ is a non-decreasing function of P_{in}, the harvested energy can be enhanced by appropriately optimizing P_{in}. However, due to the complexity of the NLM in (4), it is challenging to derive an exact closed-form expression for the average harvested energy in (5).

To this end, an upper bound on the average harvested energy at the UE under the NLM is obtained by applying Jensen's inequality, yielding

$$\bar{E}_{\mathrm{NLM}} = \mathbb{E}\left[\alpha\Phi\left(P_{\mathrm{in}}\right)\right] \le \alpha\Phi\left(\mathbb{E}\left[P_{\mathrm{in}}\right]\right) = \hat{E}_{\mathrm{NLM}}. \tag{21}$$

Since $P_{\mathrm{in}} = \frac{\beta P_t}{\left\|\boldsymbol{\psi}_{\mathrm{p}} - \boldsymbol{\psi}_{\mathrm{u}}\right\|^2}$, the derivation of $\mathbb{E}\left[P_{\mathrm{in}}\right]$ under the three waveguide deployment schemes follows a similar procedure to that of (16) and (18) in Lemmas 3 and Lemma 4, respectively. Therefore, the detailed proof is omitted here for simplicity. ∎

Furthermore, by using the Gaussian-Chebyshev quadrature method [15], we present the closed-form expressions for the average achievable rate of the UE under the three waveguide deployment schemes in the following two lemmas.

Lemma 6. For the EDS and CDS, the average achievable rate of the UE can be approximated as

$$\bar{R}_{\varpi} \approx \frac{(1-\alpha\beta)\pi}{2\mathcal{M}\ln 2} \sum_{m=1}^{\mathcal{M}} \sqrt{1-x_m^2}\ln\left(1+\frac{\mu\bar{\gamma}e^{-\delta(h^2+y_m^2)}}{h^2+y_m^2}\right), \tag{22}$$

where $\varpi \in \{1,2\}$, $y_m = \frac{D_y x_m}{2\varpi} + \frac{D_y}{2\varpi}$, $x_m = \cos\left(\frac{(2m-1)\pi}{2\mathcal{M}}\right)$, and $\mathcal{M}$ is a finite value.

Proof: Please refer to Appendix B. ∎

Lemma 7. For the DDS, the average achievable rate of the UE can be derived as

$$\begin{aligned}\bar{R}_3 \approx \frac{(1-\alpha\beta)\Lambda^2\pi}{2\mathcal{M}\ln 2} \sum_{m=1}^{\mathcal{M}} \sqrt{1-x_m^2}\ln\left(1+\frac{\mu\bar{\gamma}e^{-\delta y_m}}{y_m}\right) \\ \times\left(\frac{1}{\Lambda\sqrt{y_m-h^2}} - \frac{1}{\Lambda^2}\right),\end{aligned} \tag{23}$$

where $y_m = \frac{\Lambda^2 x_m}{2} + \frac{2h^2+\Lambda^2}{2}$, $x_m = \cos\left(\frac{(2m-1)\pi}{2\mathcal{M}}\right)$, and $\mathcal{M}$ is a finite value.

Proof: Based on (7) and (11), the average achievable rate of the UE under the DDS can be expressed as

$$\begin{aligned}\bar{R}_3 &= (1-\alpha\beta)\mathbb{E}\left[\log_2\left(1+\frac{\mu\bar{\gamma}e^{-\delta L_3^{*}}}{L_3^{*}}\right)\right] \\ &= A\int_{h^2}^{h^2+\Lambda^2} \ln\left(1+\frac{\mu\bar{\gamma}e^{-\delta l}}{l}\right)\left(\frac{1}{\Lambda\sqrt{l-h^2}} - \frac{1}{\Lambda^2}\right)\mathrm{d}l.\end{aligned} \tag{24}$$

where $A = \frac{(1-\alpha\beta)}{\ln 2}$.

Then, similar to the proof of Lemma 6, applying the Gaussian–Chebyshev quadrature method [15] to the integral in (24) yields (23). ∎

IV. Numerical Results

This section presents Monte Carlo simulations to validate the accuracy of the derived analytical results. Unless otherwise specified, the simulation parameters are set as follows: $\sigma^2 = -90$ dBm, $f_c = 28$ GHz, $D_x = 15$ m, $D_y = 10$ m, $h = 3$ m, $\alpha = 0.8$, $\beta = 0.8$, $\eta = 1$, $\varphi = 20$ mW, $a = 100$ $/\mu$W, $b = 2.9$ μW, $\delta = 0.01$ and $\mathcal{M} = 50$. Following NTT DOCOMO's experimental prototype [5], this work assumes a dielectric waveguide with a cross-sectional dimension of a few centimeters and a pinching antenna realized by a small

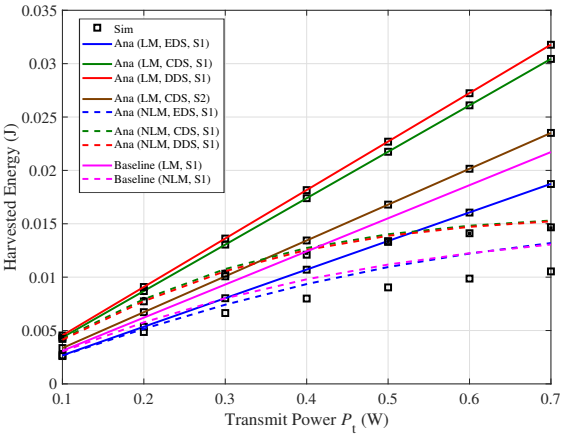

Fig. 2. The average harvested energy versus the transmit power.

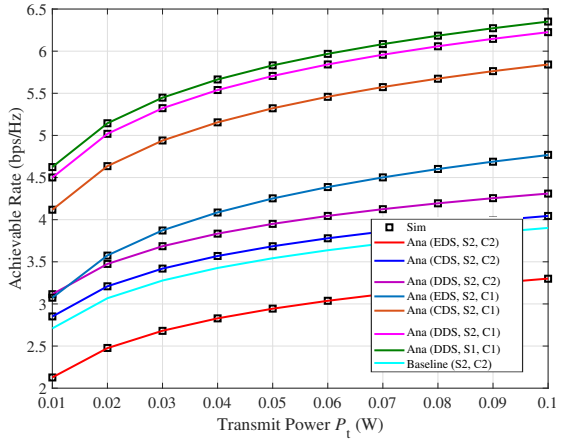

Fig. 3. The average achievable rate versus the transmit power.

dielectric attachment (on the millimeter-to-centimeter scale), both of which are practically feasible. We perform 10^6 Monte-Carlo simulations in this paper. In Figs. 2 and 3, the dashed curves represent the Monte Carlo simulation results, denoted as 'Sim', while the solid curves correspond to the analytical results, denoted as 'Ana'. Moreover, to effectively demonstrate the advantages of the proposed flexible system, we compare the derived analytical results with those of a relevant baseline scheme. Specifically, a conventional fixed antenna placed at the center of the top region of the rectangular area, i.e., at coordinates $\left(\frac{D_x}{2}, \frac{D_y}{2}, h\right)$, is considered as a simple yet representative baseline for performance comparison. The corresponding results of this baseline are illustrated by the black solid line in the figures and labeled as 'Baseline'.

Fig. 2 depicts the average harvested energy under three waveguide deployment schemes and two energy harvesting models. In addition, S1 adopts a square ground area with $D_x = 8$ m and $D_y = 8$ m, while S2 uses a rectangular ground area with $D_x = 8$ m and $D_y = 15$ m. As expected, the harvested energy increases linearly with the transmit power under the LM, whereas it gradually saturates under the NLM. It can be observed that the energy harvested by the UE under the CDS is significantly lower than that under the EDS and DDS. Moreover, under the S2 and C2 configurations, the

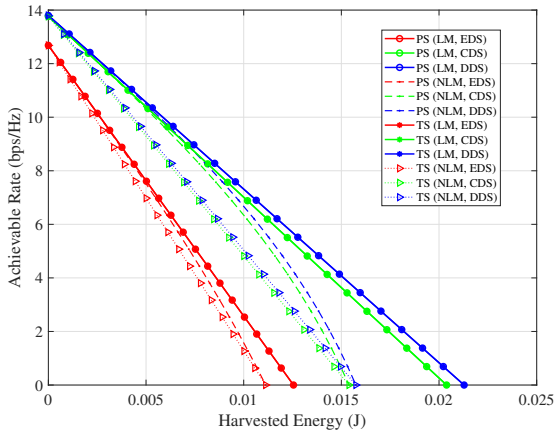

Fig. 4. Energy-rate trade-off under three waveguide deployment schemes.

baseline outperforms EDS but falls short of CDS and DDS. This is because the antenna position in EDS is constrained by equal-division placement, so the minimum achievable distance to the UE remains relatively large. In contrast, CDS/DDS place (or dynamically relocate) the pinching antenna closer to the target UE, reducing path loss and improving performance. DDS provides better performance than CDS because its diagonal layout minimizes the average antenna-to-user distance and offers more uniform coverage across the service area. Under the LM and CDS configurations, the harvested energy in the S2 scenario is lower than that in S1. This is because enlarging the room area increases the average distance between the pinching antenna and the UE, which in turn leads to higher path loss and reduced harvested energy.

Fig. 3 illustrates the average achievable rate versus the transmit power under the three waveguide deployment schemes. C1 represents the case with $\alpha = 0.8$ and $\beta = 0.8$, while C2 corresponds to $\alpha = 0.6$ and $\beta = 0.6$. It can be observed that the average achievable rate increases with the transmit power. Moreover, the performance under the C2 configuration is higher than that of C1, as more power is allocated to information decoding. These results indicate that the TS and PS coefficients strongly influence the overall system performance, and the optimal design of these parameters will be further investigated in our future work. Similar to the results in Fig. 2, the baseline scheme outperforms the EDS while exhibiting lower performance than the CDS and DDS. The DDS configuration provides a higher average achievable rate than both the EDS and CDS schemes, primarily because it results in a shorter average distance between the pinching antenna and the UE. Furthermore, under the DDS and C1 configurations, the S1 scenario achieves a higher average achievable rate than S2 because the smaller room size shortens the average separation between the pinching antenna and the UE, thereby reducing path loss.

Fig. 4 shows the energy-rate trade-off under three waveguide deployment schemes, considering both linear and non-linear energy harvesting models with TS and PS protocols. The parameters are set as follows: $P_t = 0.3$ W, $D_x = 8$ m and $D_y = 8$ m. Under the LM, the energy–rate trade-off curves are identical and exhibit linear characteristics under

both TS and PS protocols. In contrast, under the NLM, the trade-off remains linear for the TS protocol but becomes non-linear for the PS protocol. This is because, compared to the TS protocol, the PS protocol enables simultaneous energy harvesting and information decoding, thereby allowing more efficient utilization of available resources. Moreover, in a square room, the energy–rate region under the DDS outperforms those of the other two deployment schemes.

V. Conclusion

This paper investigated the performance of a novel pinching-antenna-enabled SWIPT system under three practical waveguide deployment schemes: EDS, CDS and DDS. Furthermore, a hybrid TS-PS protocol was employed to flexibly adjust the trade-off between energy harvesting and information decoding. Closed-form expressions for the average harvested energy and average achievable rate of the UE were derived under each scheme, based on the optimal positioning of the pinching antenna. Numerical results validate the analytical expressions and show that the DDS consistently outperforms the baseline and the other two deployment schemes.

Appendix A
Proof of Lemma 2

For the DDS, it is quite difficult to derive the CDF of L_3^* directly from its definition. To this end, we develop a clever approach for the derivation. As shown in Fig. 5, we first derive the CDF of the distance u between the UE and the ground projection of the pinching antenna. Therefore, we have

$$F_u(x) = \Pr\{u \le x\} = \frac{S_{ABCD}}{S_{ABE}} = 1 - \frac{S_{CDE}}{S_{ABE}}, \tag{A.1}$$

where S_Δ denotes the area of region Δ. Through analytical derivation, we obtain $\frac{S_{CDE}}{S_{ABE}} = \frac{\Lambda^2 - 2\Lambda x + x^2}{\Lambda^2}$. Then, substituting into (A.1) and simplifying yields $F_u(x) = \frac{2\Lambda x - x^2}{\Lambda^2}$. Subsequently, based on (A.1) and $F_{L_3^*}(l) = \Pr\{L_3^* \le l\} = \Pr\{u^2 + h^2 \le l\} = \Pr\{u \le \sqrt{l - h^2}\} = F_u(\sqrt{l - h^2})$, (13) can be obtained. Finally, $f_{L_3^*}(l)$ can be obtained by taking the first derivative of (13). The proof is completed.

Appendix B
Proof of Lemma 6

Based on (7) and (11), the average achievable rate of the UE under the EDS and CDS can be given by

$$\begin{aligned}\bar{R}_\varpi &= (1-\alpha\beta)\mathbb{E}\left[\log_2\left(1 + \frac{\mu\bar{\gamma}e^{-\delta L_\varpi^*}}{L_\varpi^*}\right)\right] \\ &= \frac{(1-\alpha\beta)\varpi}{2D_y \ln 2}\int_{h^2}^{h^2+\left(\frac{D_y}{\varpi}\right)^2} \ln\left(1 + \frac{\mu\bar{\gamma}e^{-\delta l}}{l}\right)\frac{1}{\sqrt{l-h^2}}\mathrm{d}l \\ &\overset{(l=h^2+t^2)}{=} \frac{(1-\alpha\beta)\varpi}{D_y \ln 2}\underbrace{\int_0^{\frac{D_y}{\varpi}} \ln\left(1 + \frac{\mu\bar{\gamma}e^{-\delta(h^2+t^2)}}{h^2+t^2}\right)\mathrm{d}\,t}_{I},\end{aligned} \tag{B.1}$$

where $\varpi \in \{1, 2\}$. However, deriving an exact closed-form expression for I in (B.1) is analytically intractable. To this end, by utilizing Gaussian-Chebyshev quadrature method [15], I_1 can be approximated as

$$I \approx \frac{D_y \pi}{2\varpi\mathcal{M}} \sum_{m=1}^{\mathcal{M}} \sqrt{1 - x_m^2} \ln\left(1 + \frac{\mu\bar{\gamma}e^{-\delta(h^2+y_m^2)}}{h^2 + y_m^2}\right), \tag{B.2}$$

where $y_m = \frac{D_y x_m}{2\varpi} + \frac{D_y}{2\varpi}$, $x_m = \cos\left(\frac{(2m-1)\pi}{2\mathcal{M}}\right)$, and $\mathcal{M}$ is a finite value.

Finally, by substituting (B.2) into equation (B.1), (22) is obtained. Here, the proof is completed.

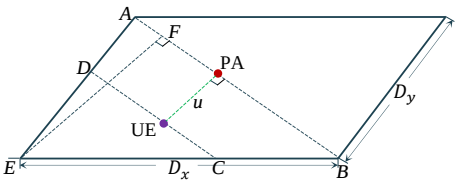

Fig. 5. The ground projection of the pinching antenna.

References

[1] J. Hu, K. Yang, G. Wen, and L. Hanzo, "Integrated data and energy communication network: A comprehensive survey," *IEEE Communications Surveys & Tutorials*, vol. 20, no. 4, pp. 3169–3219, 2018.

[2] Q. Wu and R. Zhang, "Intelligent reflecting surface enhanced wireless network via joint active and passive beamforming," *IEEE Transactions on Wireless Communications*, vol. 18, no. 11, pp. 5394–5409, 2019.

[3] K.-K. Wong, A. Shojaeifard, K.-F. Tong, and Y. Zhang, "Fluid antenna systems," *IEEE Transactions on Wireless Communications*, vol. 20, no. 3, pp. 1950–1962, 2021.

[4] L. Zhu, W. Ma, and R. Zhang, "Modeling and performance analysis for movable antenna enabled wireless communications," *IEEE Transactions on Wireless Communications*, vol. 23, no. 6, pp. 6234–6250, 2024.

[5] A. Fukuda, H. Yamamoto, H. Okazaki, Y. Suzuki, and K. Kawai, "Pinching antenna-using a dielectric waveguide as an antenna," *NTT DOCOMO Tech. J.*, vol. 23, no. 3, pp. 5–12, 2022.

[6] Y. Liu, Z. Wang, X. Mu, C. Ouyang, X. Xu, and Z. Ding, "Pinching-antenna systems (PASS): Architecture designs, opportunities, and outlook," 2025, [Online]. Available: https://doi.org/10.48550/arXiv.2501.18409.

[7] Z. Ding, R. Schober, and H. Vincent Poor, "Flexible-antenna systems: A pinching-antenna perspective," *IEEE Transactions on Communications*, pp. 1–1, 2025.

[8] Z. Zhou, Z. Yang, G. Chen, and Z. Ding, "Sum-rate maximization for NOMA-assisted pinching-antenna systems," *IEEE Wireless Communications Letters*, pp. 1–1, 2025.

[9] J. Xiao, J. Wang, and Y. Liu, "Channel estimation for pinching-antenna systems (PASS)," *IEEE Communications Letters*, pp. 1–1, 2025.

[10] D. Tyrovolas, S. A. Tegos, P. D. Diamantoulakis, S. Ioannidis, C. K. Liaskos, and G. K. Karagiannidis, "Performance analysis of pinching-antenna systems," *IEEE Transactions on Cognitive Communications and Networking*, pp. 1–1, 2025.

[11] Y. Li, J. Wang, Y. Liu, and Z. Ding, "Pinching-antenna assisted simultaneous wireless information and power transfer," *IEEE Communications Letters*, pp. 1–1, 2025.

[12] Y. Li, H. Xu, M. Zeng, and Y. Liu, "Pinching antenna-aided wireless powered communication networks," 2025, [Online]. Available: https://doi.org/10.48550/arXiv.2506.00355.

[13] R. Jiang, R. Zhang, Y. Xu, H. Hu, Y. Lu, and D. Niyato, "Spatially adaptive SWIPT with pinching antenna under probabilistic LoS blockage," 2025, [Online]. Available: https://doi.org/10.48550/arXiv.2509.03038.

[14] I. S. Gradshteyn and I. M. Ryzhik, *Table of Integrals, Series, and Products,* 7th. San Diego, CA: Academic Press, 2007.

[15] D. Kumar, P. K. Singya, O. Krejcar, K. Choi, and V. Bhatia, "On performance of intelligent reflecting surface aided wireless powered IoT network with HIs," *IEEE Communications Letters*, vol. 27, no. 2, pp. 502–506, 2023.